ORIGINAL ARTICLE

Impact of sea–land thermal contrast along the Silk Road on spring precipitation over Pamirs Plateau

Xingli Mao[1] · Li Xing[1,2] · Wei Shang[1] · Keqin Duan[1]

Abstract

The abundant precipitation over Pamirs Plateau (PP) in spring provides substantial natural and anthropogenic water resources for downstream areas. However, the factors affecting spring precipitation over PP remain unclear. Using statistical analyses and the Weather Research Forecasting (WRF) model simulations, the influence of sea–land thermal contrast along the Silk Road (Mediterranean Sea, Black Sea, Caspian Sea, Red Sea, Persian Gulf, and Turan Plain) on spring precipitation over PP was investigated. The sea–land thermal contrast is defined as sea surface temperature minus land skin temperature over Turan Plain. The spring precipitation over PP was positively correlated with the sea–land thermal contrast along the Silk Road during 1981–2018, but there was a slight difference in March, April, and May. When the sea–land thermal contrast was positive, more moisture was evaporated from the seas into the upper level (700–300 hPa) by the upward movement and transported to PP along the westerlies, which brought more precipitation over PP. When the sea–land thermal contrast was negative, the moisture from the seas transported eastward at the lower level (surface—700 hPa) and part of the moisture was lost by the high terrain along the Silk Road, resulting in less precipitation over PP. Furthermore, the WRF sensitivity simulations corroborated the positive impact of sea–land thermal contrast on the spring precipitation over PP by enhancing the water vapor content along the moisture path arriving at PP and moisture fluxes across PP. Our results emphasize that the spring precipitation over PP is influenced by the sea–land thermal contrast along the pathways of moisture sources.

Keywords Pamirs Plateau · Precipitation · Sea–land thermal contrast · WRF · HYSPLIT

1 Introduction

The water crisis has become a key constraint to the development of Central Asia (CA) as a result of increased surface temperature, decreased soil moisture in a warmer climate, and intensified agricultural drought in CA since 1922 (Cohen et al. 2012; Hansen et al. 2010; Jiang and Zhou 2023; Wang et al. 2022; Zhou et al. 2022). Pamirs Plateau (PP) acts as the water tower of CA and its precipitation plays a key role in alleviating the utilization of water resources in CA (Immerzeel et al. 2020). The precipitation over PP is the largest in spring among the four seasons (Chen et al. 2018; Huang et al. 2013), accounting for 42% of the total annual

precipitation (Aizen et al. 2001). The abundant precipitation over PP in spring increases the amount of ice and snow melting in summer (Pohl et al. 2015) and provides water for agricultural development and 1.9 billion human living in downstream areas (Immerzeel et al. 2020). Therefore, it is crucial to identify the potential factors affecting spring precipitation over PP.

More than 60% of the precipitation over land originates from the ocean (Findell et al. 2019; Van Der Ent et al. 2010). Studies reveal that the sea surface temperature (SST) anomalies in the Indian Ocean, Pacific Ocean, and Atlantic Ocean affected the precipitation over Tibetan Plateau (TP) and CA by influencing the large–scale atmospheric circulation (He et al. 2022; Hu et al. 2021a, b; Wang et al. 2019). Jiang et al. (1955) showed that during the positive phase of the tropical Pacific decadal variability, the SST anomaly in the tropical Pacific caused a significant increase in precipitation over southeastern CA during 1955–2004 through the regulation of upper and lower atmospheric circulation and moisture transportation. Yu et al. (2021) indicated that the positive

✉ Li Xing
  xingli@snnu.edu.cn

1 School of Geography and Tourism, Shaanxi Normal University, Xi'an, Shaanxi, China

2 State Key Laboratory of Loess and Quaternary Geology, Institute of Earth Environment, CAS, Beijing, China

tripole pattern of SST anomaly in the North Atlantic during winter and spring could trigger a steady downstream Rossby wave train. The cyclonic circulation over the southwestern TP carried the moisture from the Arabian Sea to western TP, which increased spring precipitation at this location. Zhao and Zhang (2016) analyzed that SST warming in the Arabian Sea was conducive to the strengthening of the southerly flow over the western Indian Ocean, which transported moisture from Indian Ocean to CA.

Land evaporation and plant transpiration accounted for 40% of the total land rainfall globally (Van Der Ent et al. 2010). Soil moisture affects the land temperature by regulating evapotranspiration (Berg et al. 2015; Yana et al. 2020; Zhou et al. 2021, 2022), and the land surface thermal conditions affects atmospheric circulation and further the precipitation over related regions (Xue et al. 2016, 2018; Yang et al. 2021; Yang and Chen 2022; Zaitchik et al. 2007). For example, Waheed et al. (2021) revealed that soil moisture in spring over TP influenced plateau precipitation by regulating the near–surface energy balance and adiabatic heating profile over TP. He et al. (2022) found that the soil moisture anomaly in the Turan Plain of CA maintained from spring to summer, leading to the atmospheric circulation anomalies over northern TP, which affected precipitation over TP.

The temporal variations of the surface temperature over the mid–latitude seas and land were different, which led to the variations of sea–land thermal contrast in different regions and affected the precipitation (Cheng et al. 2008). Chen et al. (2018) discovered that the thermal contrast between the TP and the Bay of Bengal affected the location and intensity of South Asian high pressure and Northwest Pacific subtropical high pressure by modulating the vertical circulation of the atmosphere, altering moisture transport and ultimately having a significant impact on the spatial and temporal variability of heavy rainfall events in summer over eastern China. Zhao et al. (2009) found that the northward advance of southwesterly winds and rain belt over eastern China was greatly influenced by the seasonal variations of sea–land thermal contrast between the East Asian land and its adjacent oceans. Cheng et al. (2008) suggested that the thermal contrast between mid-latitude East Asian continent and adjacent marginal seas might stimulate opposite atmospheric circulation anomalies over CA and East Asia, and affected the summer precipitation over East Asia. However, it is not clear how the sea–land thermal contrast affects the spring precipitation over PP.

The moisture sources of spring precipitation over PP mainly came from the western path along the Silk Road, including the Atlantic Ocean, Mediterranean Sea, Black Sea, Caspian Sea, Red Sea, Persian Gulf, and Turan Plain of CA (Juhlke et al. 2019; Mao et al. 2023). The seas and land conditions on the moisture path played a key role in the water vapor transportation of spring precipitation over

PP. However, the lack of vegetation cover in CA led to little contribution to atmospheric moisture by vegetation transpiration, and atmospheric moisture was dominated by evaporation of soil moisture, which changed land skin temperature and created a pressure gradient between the seas and land (Boers et al. 2017). Sea–land–air interaction is an important driving force of climate change. In the context of global change, studying the mechanism and influence of sea–land–air interaction is important to understand the mechanism of climate anomalies, properly cope with global change, and improve the level of climate prediction (Yao et al. 2019). Therefore, it is necessary to investigate the effect of sea–land thermal contrast along the Silk Road on spring precipitation over PP.

This study uses statistical methods to analyze the spatiotemporal correlation between sea–land thermal contrast along the Silk Road and spring precipitation over PP, and further explores how sea–land thermal contrast along the Silk Road affects moisture transportation and spring precipitation over the PP. Sensitive simulations to change the sea–land thermal contrast along the Silk Road with the Weather Research Forecasting (WRF) model are conducted to verify its effect on spring precipitation over PP. The remaining sections of this paper are structured as follows. Section 2 introduces the datasets, methods, and models. Section 3.1 explores the temporal variation of precipitation over PP, and Sect. 3.2 demonstrates the relationship between sea–land thermal contrast along the Silk Road and spring precipitation over PP, and the possible mechanisms are further discussed in Sect. 3.3. Section 3.4 presents the results of numerical experiments. Finally, conclusions and discussion are given in Sect. 4.

2 Datasets, methods, and models

2.1 Datasets

The Global Precipitation Climatology Centre (GPCC) (Becker et al. 2013) with a spatial resolution of 0.25°×0.25° from 1981 to 2018 and the Global Precipitation Measurement (GPM) dataset (https://gpm.nasa.gov/data/directory) with a horizontal resolution of 0.1°×0.1° from 2001 to 2018 were used to analyze the temporal variation of monthly precipitation over PP and verify the model performance of precipitation over PP by WRF. The SST was derived from the monthly–mean Hadley Centre Global Sea Ice and SST (HadISST) dataset (Rayner et al. 2003) with a horizontal resolution of 1°×1° from 1981 to 2018. The skin temperature, soil moisture, and snow melt from the fifth generation ECMWF reanalysis (ERA5–Land) dataset (https://cds.climate.copernicus.eu/) with a horizontal resolution of 0.1°×0.1° from 1981 to 2018 were downloaded to analyze the temporal

variation of the precipitation over PP, land surface temperature, soil moisture, and snow melt in the Turan Plain of CA. Atmospheric variables, including specific humidity, horizontal velocity, and surface pressure from ERA5 dataset (https://cds.climate.copernicus.eu/) with a horizontal resolution of 0.25°×0.25° from 1981 to 2018 were employed to analyze the atmospheric moisture and circulations. The Objectively Analyzed air–sea Fluxes (OAFlux) for the Global Oceans dataset (http://oaflux.whoi.edu/index.html) with a horizontal resolution of 1°×1° from 1981 to 2018 was used to calculate the evaporation rates over the five seas.

2.2 Methods

The study domain includes PP (32° N–42° N, 68° E–78° E), Turan Plain (30° N–43° N, 55° E–65° E), and the five seas (Mediterranean Sea, Black Sea, Caspian Sea, Red Sea, and Persian Gulf) along the Silk Road, as shown in Fig. 1. We defined the sea–land thermal contrast index by calculating the SST of the Mediterranean Sea, Black Sea, Caspian Sea, Red Sea, and Persian Gulf minus the land skin temperature of Turan Plain following Eq. (1):

$$I = T_s - T_l \tag{1}$$

where I was the sea–land thermal contrast index along the Silk Road, T_s was the mean SST for each of the five seas, and T_l was the mean skin temperature of Turan Plain. Five sea–land thermal contrast indices, expressed as MTTCI (Mediterranean Sea–Turan Plain Thermal Contrast Index), BTTCI (Black Sea–Turan Plain Thermal Contrast Index), CTTCI (Caspian Sea–Turan Plain Thermal Contrast Index),

RTTCI (Red Sea–Turan Plain Thermal Contrast Index), and PTTCI (Persian Gulf–Turan Plain Thermal Contrast Index), were used for further analyses.

The correlations between the thermal contrast index and the monthly–mean precipitation over PP in MAM (March, April, and May) from 1981 to 2018 were calculated and the Student's t test was used to verify the significance of the correlations. The linear trends for the precipitation over PP, SST of the five seas, and skin temperature of Turan Plain in MAM were removed before the correlation analyses.

To explore the impact of sea–land thermal contrast on precipitation, we selected three positive and three negative sea–land thermal contrast along the Silk Road, precipitation over PP, and vertical velocity at the lower level (surface–700 hPa) over the five seas years during 1981–2018 in March (2007/2014/2015 and 2001/2004/2008), April (2009/2013/2016 and 2000/2001/2010), and May (1992/2003/2018 and 2006/2008/2017) over PP (Fig. S1). The composite analyses were used to examine the anomalies of atmospheric circulations and moisture flux in the selected years. The selected years must meet the criteria that the anomalies of precipitation and sea–land thermal contrast index must be simultaneously positive or negative, the anomaly of vertical velocity must be opposite to sea–land thermal contrast index and precipitation, and the anomalies of the three variables must exceed their own standard deviation. There were two negative years in April and two positive years in May that meet the criteria. In order to keep consistent with the composite analyses of three years in March, we also chose 2010 in April and 2003 in May for composite analyses. In April 2010, the precipitation and vertical velocity met the criteria and the sea–land thermal contrast index

Fig. 1 The terrain height (m) of WRF domain. The thick white line represents the five seas and the altitude contour line of 3000 m over TP, and the gray box represents the region of Turan Plain for the soil moisture calculation. The black box represents PP, and the black points represent 16 target points for the calculation of HYSPLIT. Red lines denote the section A (30° N–43° N, 28° E) and section B (30° N–43° N, 68° E), respectively
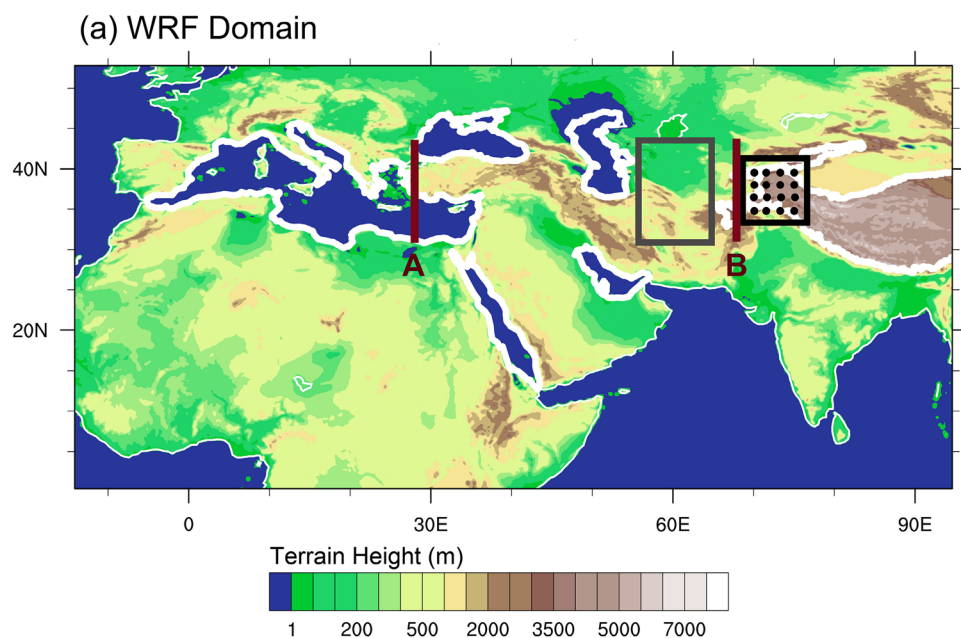
was close to the standard deviation and did not exceed it. In May 2003, the positive anomaly of the sea–land thermal contrast index was the largest and the negative anomaly of the vertical velocity was larger, both exceeding the standard deviation, while the positive anomaly of precipitation was close to the standard deviation and did not exceed the standard deviation.

We calculated the composite moisture flux in the upper and lower layers during the three positive and negative years across the section A (30° N–43° N, 28° E) and section B (30° N–43° N, 68° E) (as shown in Fig. 1) in MAM as follows:

$$Q_z = -\frac{1}{g} \int_{Ps}^{Pt} \overrightarrow{U} q dp \tag{2}$$

where Q_z was the zonal moisture flux, g was gravitational acceleration (9.8 m/s^2), $\overrightarrow{U}$ was the zonal wind velocity vector at each pressure layer, and q was the specific humidity at each pressure layer. Pt and Ps were the upper and lower bounds of the atmosphere for calculating Q_z, respectively. We defined the upper layer as 700–300 hPa and the lower layer as surface–700 hPa.

We also calculated the column moisture fluxes across the boundaries of PP. The moisture fluxes across the eastern and western boundaries over PP were calculated following Eq. (2), and the moisture fluxes across the northern and southern boundaries over PP were calculated following:

$$Q_m = -\frac{1}{g} \int_{Ps}^{Pt} \overrightarrow{V} q dp \tag{3}$$

where Q_m was the meridional moisture flux, and $\overrightarrow{V}$ was the meridional wind velocity vector at each pressure layer. Ps and Pt were from the surface to the top of the atmosphere.

To investigate the relationship between moisture and precipitation, we calculated the column moisture flux convergence over PP in MAM in positive and negative years and in the Seas_Warming and Seas_Cooling experiments as follows:

$$MFC = \frac{1}{g} \int_{Pt}^{Ps} \nabla \cdot (uq + vq) dp \tag{4}$$

where MFC was vertically integrated moisture flux divergence, g was gravitational acceleration (9.8 m/s^2), Ps and Pt were from the surface to the top of the atmosphere, u was the zonal wind velocity vector at each pressure layer, v was the meridional wind velocity vector at each pressure layer, and q was the specific humidity at each pressure layer. When MFC < 0, it means that moisture converges, which is conducive to convection and precipitation. When MFC > 0, it means that moisture diverges, which is not conducive to precipitation.

2.3 Models

The Hybrid Single–Particle Lagrangian Integrated Trajectory (HYSPLIT) model (Stein et al. 2015) was used to calculate backward trajectories at 16 target points (as shown in the small black box in Fig. 1) at 200 m above the ground level over PP in MAM, which was driven with the meteorological input from the Global Data Assimilation System (GDAS) dataset (ftp://arlftp.arlhq.noaa.gov/pub/archives/gdas1) with 1°×1° spatial resolution. For each backward trajectory at each target point, the latitude, longitude, and pressure along the trajectory were recorded every hour for ten days (240 h). The backward trajectories were calculated on each day in spring in the selected years (the same as the years selected for the composite analyses) and the pressure along the backward trajectories were further analyzed.

WRF version 4.0 with the Advance Research dynamic solver was used to investigate the sea–land thermal contrast along the Silk Road on the spring precipitation over PP. The FNL data (http://rda.ucar.edu) with 1°×1° horizontal resolution and 6h interval from the National Centers for Environmental Prediction (NCEP) were used as the initial and boundary conditions of the WRF model. Table 1 shows the model experimental scheme design. The model chose the Single-Moment 6-class microphysical scheme (Hong and Lim 2006), the Betts–Miller–Janjic cumulus parameterization (Janjic 2001), Community Atmosphere Model for shortwave and long wave radiation (Collins et al. 2004), and the Noah land surface model (Skamarock et al. 2008).

The numerical simulations consist of the control (CTL) and sensitivity experiments, as shown in Table 1. The SST input for the CTL were driven by the National Centers for Environmental Prediction Global Forecast System (NCEP GFS) dataset (https://doi.org/10.5065/D65D8PWK) with horizontal resolution of 0.25°×0.25°. Since the SST data started from 2015, we chose the years after 2015 that met the criteria that the sea–land thermal contrast index and precipitation were close to the climatological mean values and simultaneously had positive or negative anomalies, which were March 2018, April 2017, and May 2015. Ten days in advance each month were also simulated and regarded as spin-up time. The sensitivity experiments remained the same as the CTL, except that the SST over the five seas (Seas_Warming and Seas_Cooling) and skin temperature over the Turan Plain (Land_Warming and Land_Cooling) increased and decreased by 5 ℃, respectively, as the anomalies of sea–land thermal contrast index in MAM were between + 5 ℃ and − 5 ℃ (Fig. S2). The Seas_Warming and Land_Cooling simulations both represented the increased sea–land thermal contrast, while the Seas_Cooling and Land_Warming both represented the decreased sea–land thermal contrast. The difference between the sensitivity and

Table 1 WRF experimental scheme design

Simulation domain	D01 (as shown in Fig. 1)
Simulation period	March 2018/April 2017/May 2015
Simulation center	29.9° E, 40.2° N
Horizontal resolution	15 km
Lattice dimension	700×400
Microphysical scheme	Single–Moment 6–class (Hong and Lim 2006)
Shortwave radiation	Community Atmosphere Model (Collins et al. 2004)
Longwave radiation	Community Atmosphere Model (Collins et al. 2004)
Cumulus parameterization	Betts–Miller–Janjic (Janjic 2001)
Land surface process	Noah (Skamarock et al. 2008)
Control experiments (CTL)	SST driven by the NCEP GFS dataset
Seas_Warming	+5 ℃ SST over the Mediterranean Sea, Black Sea, Caspian Sea, Red Sea, and Persian Gulf
Seas_Cooling	− 5 ℃ SST over the Mediterranean Sea, Black Sea, Caspian Sea, Red Sea, and Persian Gulf
Land_Warming	+5 ℃ skin temperature over the Turan Plain
Land_Cooling	− 5 ℃ skin temperature over the Turan Plain

CTL experiments reflects the impact of sea–land thermal contrast along the Silk Road on spring precipitation over PP.

3 Results

3.1 Temporal and spatial variations of monthly precipitation over PP

Figure 2 shows the temporal variations of monthly average precipitation over PP from 1981 to 2018 (ERA5–Land and GPCC), and from 2001 to 2018 (GPM). The seasonal precipitation in PP was the largest in spring with 209.5/157.7/150.2 mm (ERA5–Land/GPCC/GPM), followed by 147.9/112.9/127.1 mm (ERA5–Land/GPCC/GPM) in winter, 101.3/70.1/55.1 mm (ERA5–Land/GPCC/GPM) in summer, and 88.8/55.8/58.3 mm (ERA5–Land/GPCC/GPM) in autumn, respectively. The monthly precipitation in spring over PP was the largest in March (78.0/62.5/59.8 mm (ERA5–Land/GPCC/GPM)), and the lowest in May (60.6/40.7/37.3 mm (ERA5–Land/GPCC/GPM)). The monthly precipitation in April was 70.9/54.5/53.2 mm (ERA5–Land/GPCC/GPM). Figure S3 shows the spatial variations of seasonal and spring monthly average precipitation over PP from 1981 to 2018 (ERA5–Land and GPCC), and from 2001 to 2018 (GPM). The precipitation in spring and winter was concentrated in the north, west and south of PP. The precipitation in summer and autumn was mainly

Fig. 2 The temporal variations of monthly average precipitation (mm) over PP from 2001 to 2018 (GPM), from 1981 to 2018 (GPCC), and from 1981 to 2018 (ERA5–Land)
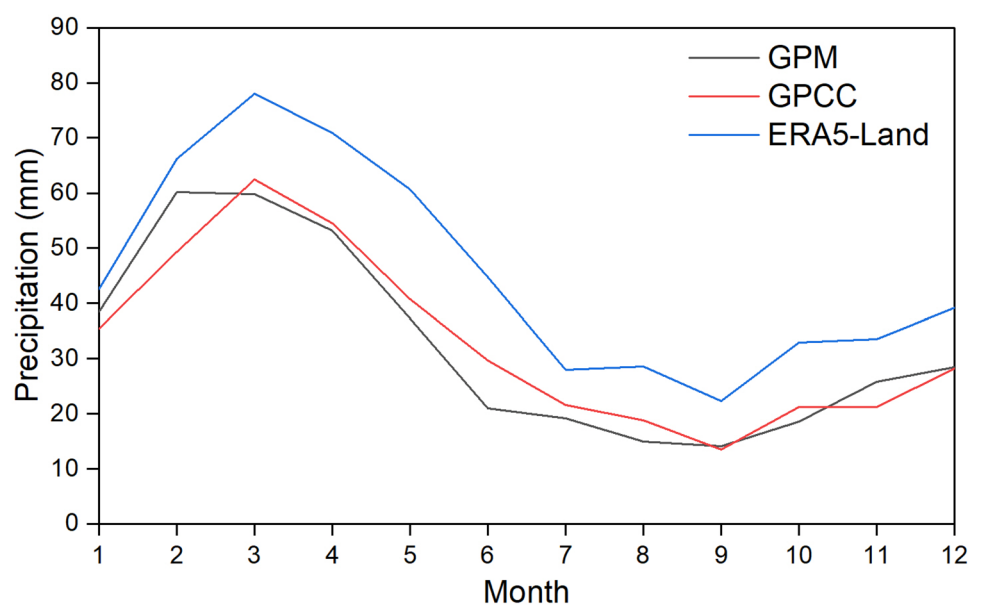
concentrated in the south of PP. The spatial distributions of precipitation in March, April, and May were consistent with that in spring. We further analyzed how the sea–land thermal contrast along the Silk Road influenced the monthly precipitation over PP in spring.

3.2 Relationship between sea–land thermal contrast along the Silk Road and spring precipitation over PP

To explore the relationship between sea–land thermal contrast along the Silk Road and spring precipitation over PP, we analyzed their temporal and spatial correlations, respectively. Figure 3 presents the time series of the sea–land thermal contrast indices along the Silk Road and precipitation over PP in MAM from 1981 to 2018. All the five sea–land thermal contrast indices were significantly positively correlated with the precipitation over PP in MAM, with the correlation coefficients ranging from 0.38 to 0.50. The sea–land contrast indices in the west of PP (MTTCI, BTTCI, and CTTCI) were larger in March and April (0.39–0.50) than those in May (0.38–0.45), but the indices in the southwest of PP (RTTCI and PTTCI) were larger in May (0.44–0.50) than those March and April (0.41–0.47). The results indicated that the precipitation over PP was more influenced by the moisture from the west path in March and April, and the moisture contribution from the southwest of PP was higher in May, with the onset of Indian monsoon (Hu et al. 2021a, b).

Figure 4 shows the spatial correlations of the sea–land thermal contrast indices along the Silk Road and the gridded precipitation over PP in MAM from 1981 to 2018, and the areas with significant correlation are shown. The sea–land thermal contrast along the Silk Road was positively correlated with spring precipitation over PP. The spatial distributions of correlations for different sea–land thermal contrast indices were consistent in the same month, but there were differences among different months. Figure 4a1–e1 show that in March, the sea–land thermal contrast along the Silk Road had the greatest influence on the precipitation in the central, southwestern, and southeastern PP. In April, the significant correlation coefficients primarily occurred over the northwestern PP (Fig. 4a2–e2). However, areas with significant correlations in May were mainly distributed over the central and western PP (Fig. 4a3–e3).

3.3 Possible mechanisms for the sea–land thermal contrast along the Silk Road affecting spring precipitation over PP

### 3.3.1 Moisture sources of spring precipitation over PP and atmospheric circulation

The above correlation analyses indicated that when the sea–land thermal contrast indices along the Silk Road were positive, there were more precipitation over PP, and when sea–land thermal contrast indices along the Silk Road were negative, the precipitation over PP were less. To verify the atmospheric circulations generated by the sea–land thermal contrast along the Silk Road, we used the HYSPLIT model to analyze the average pressure along the backward trajectories during the three positive and three negative precipitation years (as selected in Sect. 2.2) over PP in MAM. Figure 5 shows that the pressure along the backward trajectories in the positive precipitation years was generally lower than those in negative precipitation years. Figure 5a, b show that in March and April, the average pressure along the backward trajectories were 690 hPa and 670 hPa in the positive precipitation years, respectively, while they were 720 hPa and 700 hPa in the negative precipitation years, respectively. Figure 5c shows that the pressure along the backward trajectories in the positive and negative precipitation years did not vary much during the initial eight days and the pressure was lower in the positive precipitation years than that in the negative precipitation years during the ninth and tenth days, which displayed the different characteristics with that in March and April. The reason might be that May is the transition month between spring and summer, and the Indian summer monsoon started to influence the precipitation over PP, and the water vapor from the western path was no longer the dominant source of the precipitation over PP. Figure S4 also shows that the backward trajectories in March and April mainly came from the west of PP, while there were more trajectories originating from the southwest of PP in May. The above results indicated that the atmospheric circulations varied greatly between the positive and negative precipitation years.

Water vapor transportation is mainly affected by atmospheric circulations. Figure 6 shows the composite anomalies of wind fields and specific humidity at the upper layer in the positive precipitation years and at the lower layer in the negative precipitation years. When the sea–land thermal contrast along the Silk Road and precipitation was positive, the specific humidity over PP in MAM was positively anomalous at the upper level. In March (Fig. 6a1), abnormal SST warming can trigger eastward–propagating wave train along the westerlies, which caused the anomalous cyclone and anticyclone over North Africa, facilitating the moisture transportation from the Mediterranean Sea, Red Sea,
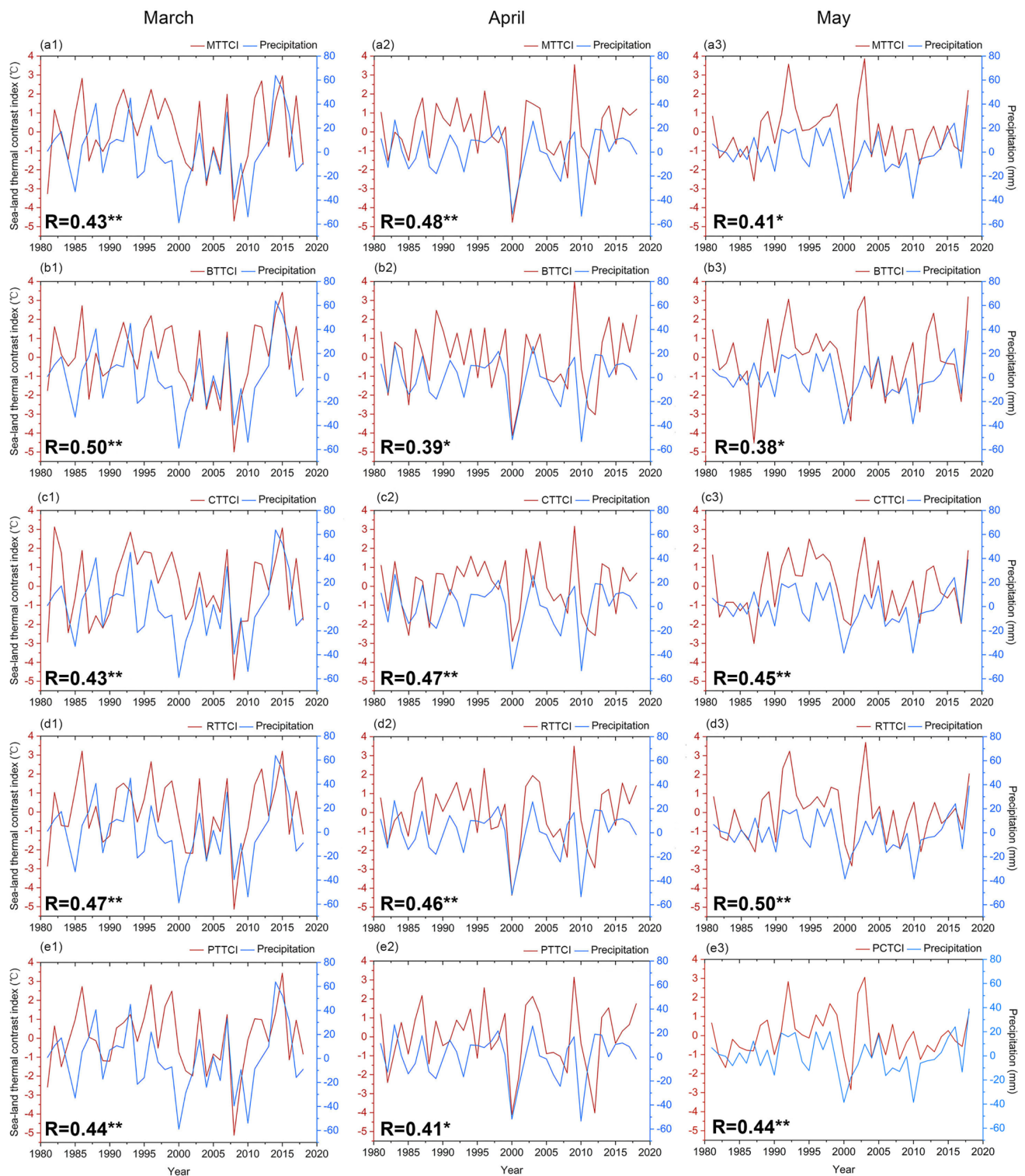
Fig. 3 The time series of **a1**–**a3** MTTCI, **b1**–**b3** BTTCI, **c1**–**c3** CTTCI, **d1**–**d3** RTTCI, **e1**–**e3** PTTCI, and the monthly precipitation (GPCC) over PP in MAM from 1981 to 2018. One asterisk (*) and double asterisks (**) indicate that the correlation coefficients are significant at the 95% and 99% confidence levels based on Student's *t* test, respectively
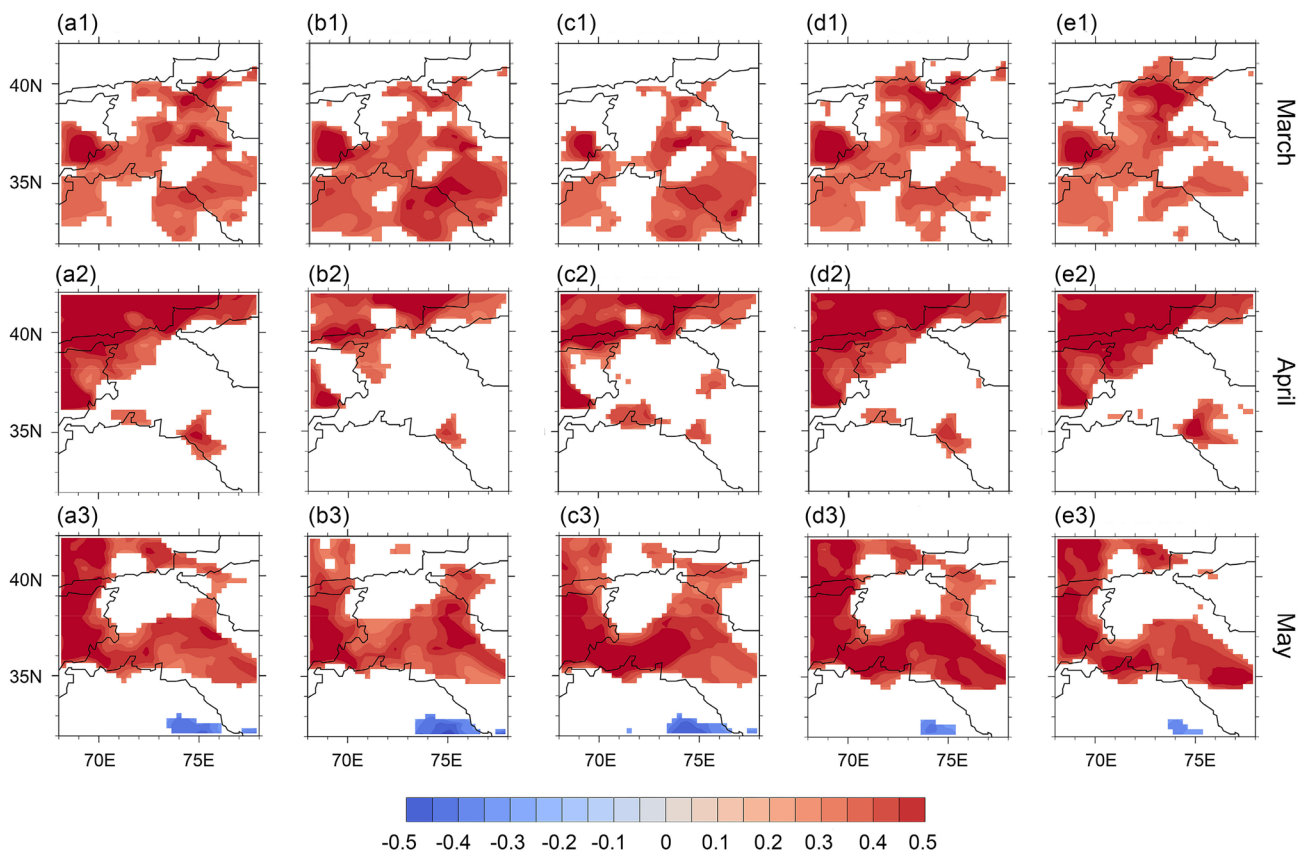
Fig. 4 The spatial distributions of correlations between the precipitation over PP and **a1**–**a3** MTTCI, **b1**–**b3** BTTCI, **c1**–**c3** CTTCI, **d1**–**d3** RTTCI, and **e1**–**e3** PTTCI in MAM from 1981 to 2018. Only areas that were significantly correlated are shown. The black outlines represent the contour line of 3000 m
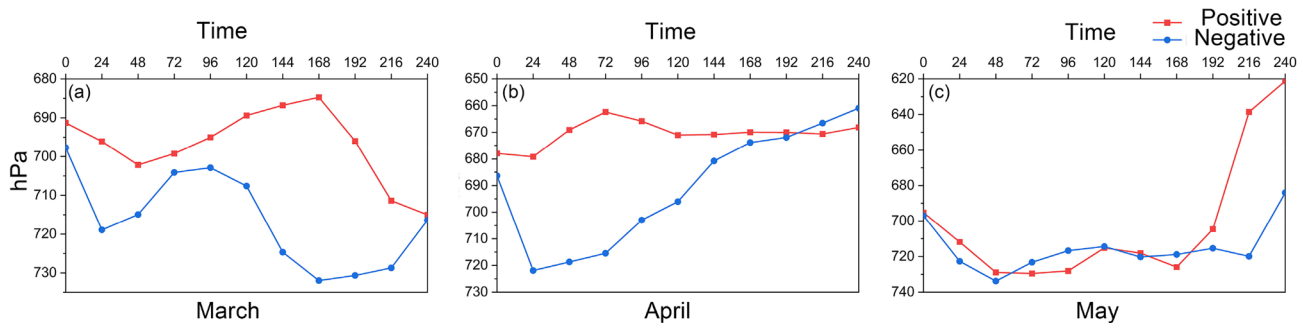

Fig. 5 The average pressure (hPa) along the backward trajectories during the positive and negative precipitation years over PP in **a** March, **b** April, and **c** May

Caspian Sea, and Persian Gulf to PP (Fig. S6a1). This wave train also caused cyclonic anomalies in the southwestern PP, enhancing upper–level divergence and providing favorable conditions for precipitation over PP. In April (Fig. 6b1), the anomalous anticyclone spanning in Europe carried water vapor from the Mediterranean Sea, Black Sea, and Red Sea to PP (Fig. S6b1). The strong anomalous cyclone over the west of PP increased precipitation over PP. In May (Fig. 6c1

and Fig. S6c1), the large–scale anticyclone in central Asia and PP did not facilitate the precipitation increase over PP, but the moisture flux in southern PP and specific humidity in PP was slightly increased, which enhanced the precipitation in PP. At the lower layer in MAM of positive anomalies years (Figs. S5a1, b1, c1), there were wind fields anomalies blowing from land to seas, and moisture fluxes were also negative anomalies in MAM (Figs. S7a1, b1, c1). However,
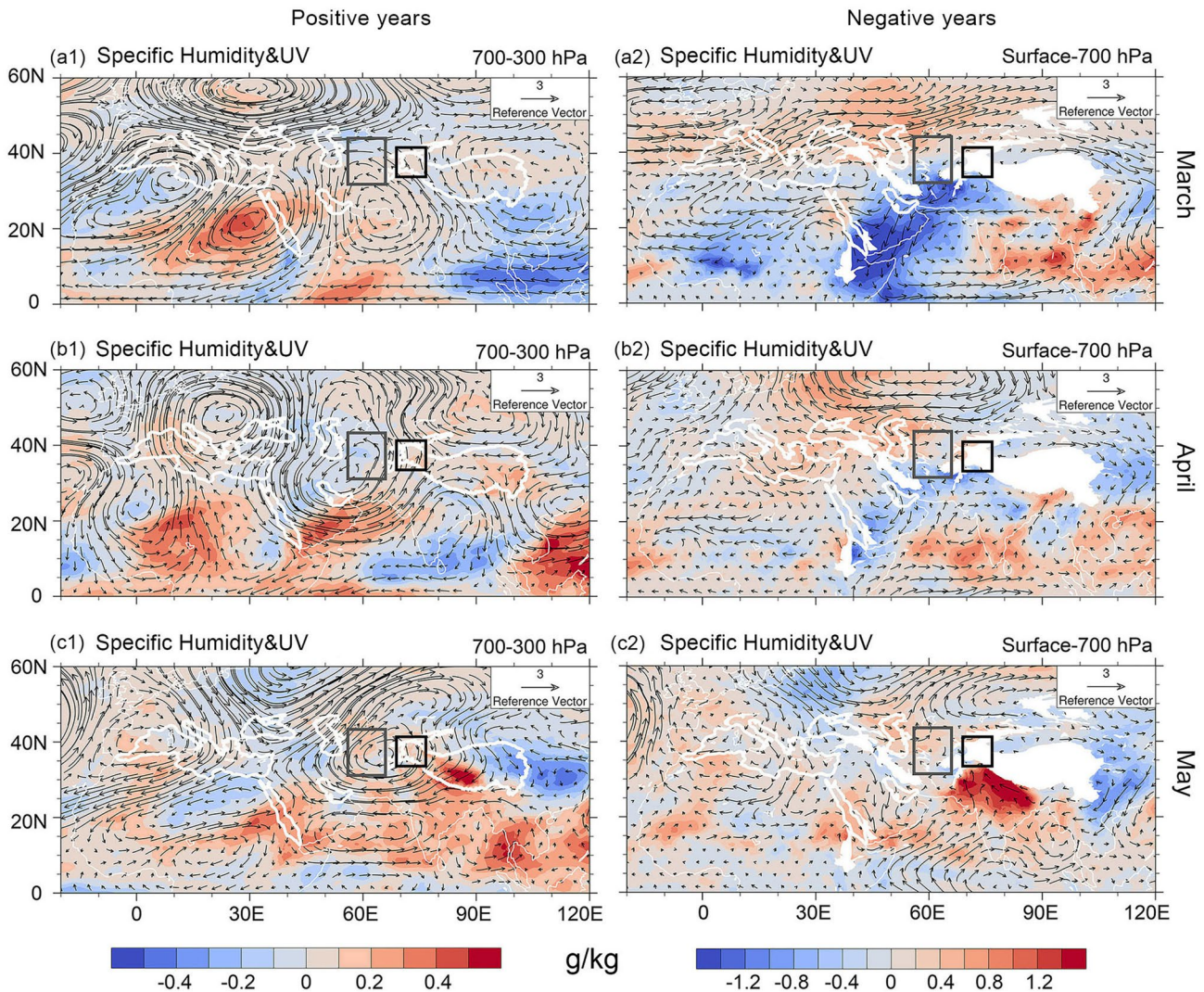
Fig. 6 Three years composite analyses of wind fields (m/s) and specific humidity (g/kg) anomalies in **a1** March, **b1** April, and **c1** May at the upper layer (700–300 hPa) in the years of positive anomalies of sea–land thermal contrast along the Silk Road, and in **a2** March, **b2** April, and **c2** May at the lower layer (surface–700 hPa) in the years of negative anomalies of sea–land thermal contrast along the Silk Road. The white lines represent the altitude contour line of 3000 m over TP and five seas. The gray box represents Turan Plain and the black box represents PP

at the upper layer in MAM of negative anomalies years (Figs. S5a2, b2, c2), there were anticyclonic anomalies over the Turan Plain, which indicated that the higher land skin temperature and lower SST resulted in abnormal high pressure at high altitudes and transported water vapor to the seas (Figs. S7a2, b2, c2). At the lower layer, there were negative specific humidity anomalies at the southwest of PP in March (Fig. 6a2) and April (Fig. 6b2), and slightly less in May (Fig. 6c2). Except for the south wind anomaly from the Indian Ocean in May, which transported water vapor to PP (Fig. S6c2), the wind anomalies in March and April were not conducive to water vapor transportation to PP (Fig. S6a2, b2).

In addition, the composite anomalies of vertical velocity at the lower layer in the positive precipitation years and negative precipitation years were calculated. The results show that the average vertical velocity over the five seas was abnormally upward (− 0.0042 Pa/s, − 0.0028 Pa/s, and − 0.0038 Pa/s) in MAM in the positive years, while it was abnormally downward (0.0025 Pa/s, 0.0024 Pa/s, and 0.00017 Pa/s) in MAM in the negative years. Meanwhile, the composite anomalies of evaporation rate from five seas in MAM in positive and negative precipitation years were calculated. The results show that the difference of evaporation anomalies between positive and negative years were positive (11.1 cm/yr in March, 3.8 cm/yr in April, 4.6 cm/yr in May).

The above results indicated that when the sea–land thermal contrast was positive, the upward movement of water vapor was more favorable and the atmospheric circulations facilitated the moisture transportation to PP in the upper level and resulted in more precipitation over PP. When the sea–land thermal contrast was negative, the downward movement of water vapor and atmospheric circulations inhibited the transportation of water vapor to PP and caused less precipitation over PP.

3.3.2 Moisture fluxes and convergence over PP

In order to quantitatively investigate the water vapor transportation over PP, we calculated the composite moisture fluxes at the upper and lower layers in the three positive and three negative anomalous years of sea–land thermal contrast along the Silk Road across section A (30° N–43° N, 28° E) and section B (30° N–43° N, 68° E) (as shown in Fig. 1) following Eq. (2). Table 2 shows that at the upper layer in the positive years, the moisture fluxes from section A to section B increased from 426.4 to 539.2 g/m·s in March, followed by that from 454.4 to 615.2 g/m·s in April, and from 340.8 to 617.6 g/m·s in May. The results indicated that when the sea–land thermal contrast along the Silk Road was positive, the moisture over the upper layer was enhanced from section A to section B due to moisture supplement evaporated from the higher SST along the Silk Road and upward movement, resulting in more precipitation over PP. At the lower layer in the positive years, higher SST in section A resulted in the greater moisture fluxes over the seas (section A) than that on land (section B) in March and April, while the water vapor in May came mainly from the Red Sea and the Persian Gulf, which increased the moisture arriving at PP. Therefore, the moisture fluxes in section A was less than that in section B in May.

In contrast, the amount of water vapor transportation at the lower layer in the negative years depleted from section A to section B, and the depleting rates in MAM were 54.6%, 41.9%, and 34.7%, respectively, which was probably caused by the terrain increase in Iran and Turkey, inhibiting the moisture transportation to PP. When the sea–land thermal contrast along the Silk Road was negative, the moisture transportation from sea to land at the lower layer decreased, resulting in less precipitation over PP. At the upper layer in the negative years, higher land skin temperature in April and May evaporated soil moisture to higher layer, making the moisture fluxes at upper level greater in section B than in section A, but the enhancement was generally smaller than that in the positive years. The moisture flux in March was much smaller than that in April and May, which may be due to the lower land skin temperature, compared to that in April and May.

Moreover, the moisture flux convergence anomalies over PP in MAM in positive and negative years were calculated following Eq. (4). Fig. S18 shows that the moisture flux convergence differences in MAM between positive and negative years were negative [-2.8×10^{-7} kg/(m^2·s), -0.5×10^{-7} kg/(m^2·s), -1.5×10^{-7} kg/(m^2·s)], which indicated that positive years were more conducive to water vapor convergence and precipitation.

3.4 Numerical simulation results

3.4.1 The verification of model performance

The numerical experiments were conducted to verify the impact of the sea–land thermal contrast along the Silk Road on the spring precipitation over PP. The model performance of the CTL by WRF on the specific humidity, atmospheric circulations, and precipitation in MAM were evaluated.

Table 2 The moisture fluxes (g/m · s) across the section A (30° N–43° N, 28° E) and section B (30° N–43° N, 68° E) and their depleting rate at the upper and lower layers during the positive and negative years of sea–land thermal contrast along the Silk Road and precipitation in MAM

Month	Unit: g/m · s		A (30° N–43° N, 28° E)	B (30° N–43° N, 68° E)	Depleting rate (%)
March	Positive years	700–300 hPa	426.4	539.2	
		Surface–700 hPa	650.4	429.6	
	Negative years	700–300 hPa	574.4	479.2	
		Surface–700 hPa	956.0	433.6	54.6
April	Positive years	700–300 hPa	454.4	615.2	
		Surface–700 hPa	614.4	520.8	
	Negative years	700–300 hPa	593.6	618.4	
		Surface–700 hPa	932.0	541.6	41.9
May	Positive years	700–300 hPa	340.8	617.6	
		Surface–700 hPa	302.4	614.4	
	Negative years	700–300 hPa	496.0	584.0	
		Surface–700 hPa	790.4	516.0	34.7

Figure S8 shows the spatial distribution of precipitation in March 2018 derived from GPCC, GPM, and WRF model simulation. In the whole study area, the precipitation concentrated around the Europe, Mediterranean Sea, Black Sea, Caspian Sea, and PP. The WRF (Figs. S8c1 and c2) simulations reproduced the spatial distribution of observed precipitation from GPCC (Figs. S8a1 and a2) and GPM (Figs. S8b1 and b2). WRF can depict the precipitation changes over the complex terrain more accurately due to the high resolution. Figure S10 and Figure S12 also show the good performance of spatial distributions of precipitation by the WRF model in April 2017 and May 2015. The average precipitation over PP from GPCC, GPM, and WRF were 40.7 mm, 40.2 mm, and 63.4 mm in March, 63.2 mm, 54.5 mm, and 81.6 mm in April, and 54.0 mm, 46.9 mm, and 73.7 mm in May, respectively. We calculated the spatial correlations of precipitation between WRF and GPCC/GPM in the WRF domain. The correlation coefficients in March, April, and May were 0.79/0.77 (WRF&GPCC/WRF&GPM), 0.50/0.40 (WRF&GPCC/WRF&GPM), and 0.43/0.43 (WRF&GPCC/WRF&GPM), respectively, all of which passed the 95% significance test. WRF model generally overestimated precipitation over PP, which has been revealed in previous studies that WRF model usually overestimated precipitation in the plateau (Bao et al. 2015; Cai et al. 2023; Tian et al. 2020; Zhou et al. 2023). The horizontal resolution and physical parameterization scheme can lead to the overestimation of precipitation in WRF model.

Figure S9, Figure S11, and Figure S13 present the specific humidity overlaid by wind fields from ERA5 reanalysis data and WRF model simulation at 500 hPa and 850 hPa in March 2018, April 2017, and May 2015, respectively. WRF model well reproduced the spatial distributions of specific humidity and wind fields at 500 hPa and 850 hPa in MAM, compared to the results from ERA5. Therefore, the CTL simulation from WRF model was reliable and can be used for further studies in sensitivity experiments.

3.4.2 Simulated moisture, moisture transport, and precipitation

Firstly, the differences in the specific humidity between the CTL and Seas_Warming/Seas_Cooling (the latter minus the former) were investigated. When the SST was warmed, the total column water vapor over the five seas always increased. The total column water vapor over PP also increased in March (Fig. S14a1) and in April (Fig. S14b1), except for a slight decrease over the northern PP. In May (Fig. S14c1), the spatial distributions of total column water vapor differed greatly with that in March and April, indicating that the transition of atmospheric circulation patterns (i.e. the onset of Indian summer monsoon) influenced the response of water vapor to SST change. The total column water vapor mainly increased over the southeastern PP in May. When the SST was cooled, the water vapor over PP and the five seas decreased in MAM (Figs. S14a2, b2, c2), except for a small increase over the southeastern PP.

We also quantified moisture fluxes at the upper and lower layers for the Seas_Warming and Seas_Cooling. Table 3 illustrates that when SST was warmed, the moisture fluxes at the upper layer increased from section A to section B, which were from 410.4 to 560.0 g/m·s in March 2018, from 321.6 to 431.2 g/m·s in April 2017, and from 287.2 to 606.4 g/m·s in May 2015. When the SST was cooled, the moisture fluxes at the lower layer decreased from section A to section B in MAM, with depleting rate of 40.0%, 24.6%, and 27.8%, respectively. The above simulation results were consistent with the observation results shown in Table 2, which further verified the key role of sea–land thermal contrast along the Silk Road on moisture transportation.
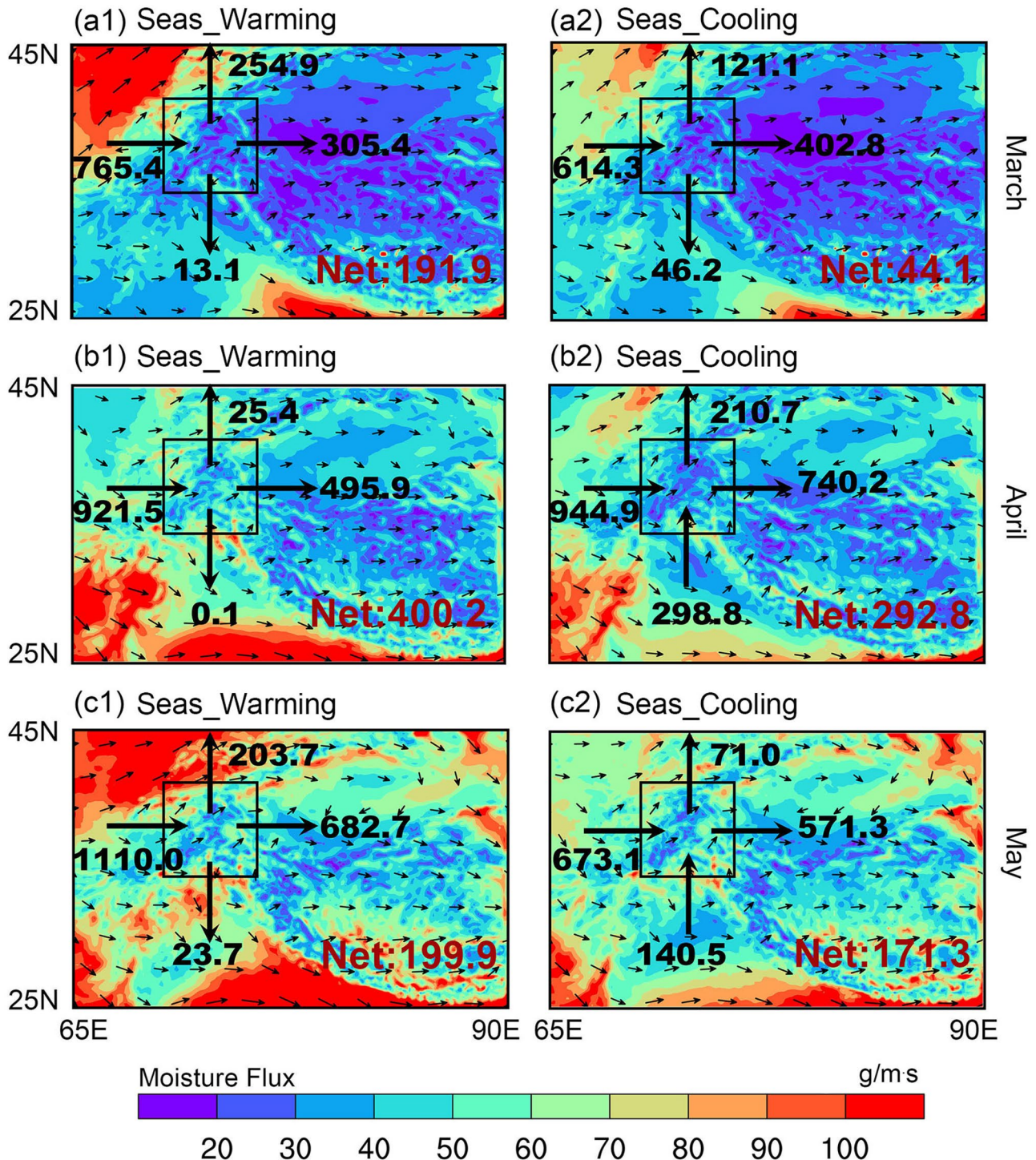
Table 3 The moisture fluxes (g/m·s) across the section A (30° N–43° N, 28° E) and section B (30° N–43° N, 68° E) and their depleting rate at the upper and lower layers in the SST sensitivity experiments (Seas_Warming and Seas_Cooling) in MAM

Month	Unit: g/m·s		A (30° N–43° N, 28° E)	B (30° N–43° N, 68° E)	Depleting rate (%)
March 2018	Seas_Warming	700–300 hPa	410.4	560.0	
		Surface–700 hPa	812.0	437.6	
	Seas_Cooling	700–300 hPa	488.8	397.6	
		Surface–700 hPa	513.6	308.0	40.0
April 2017	Seas_Warming	700–300 hPa	321.6	431.2	
		Surface–700 hPa	367.2	312.0	
	Seas_Cooling	700–300 hPa	299.2	439.2	
		Surface–700 hPa	285.6	215.2	24.6
May 2015	Seas_Warming	700–300 hPa	287.2	606.4	
		Surface–700 hPa	480.8	440.8	
	Seas_Cooling	700–300 hPa	320.0	463.2	
		Surface–700 hPa	334.4	241.6	27.8

In addition, the net total column moisture fluxes across PP for the Seas_Warming and Seas_Cooling experiments in MAM were quantified. Figure 7 shows that the net moisture fluxes over the PP were significantly higher for the Seas_Warming experiment than those for the Seas_Cooling experiment in March and April, which were 191.9 g/m·s for the Seas_Warming and 44.1 g/m·s for the Seas_Cooling in March, 400.2 g/m·s for the Seas_Warming and 292.8 g/m·s for the Seas_Cooling in April. The difference was much smaller in May, with moisture fluxes of 199.9 g/m·s for the

Fig. 7 The moisture fluxes (g/m·s) across the four boundaries over PP in the SST sensitivity experiments in MAM. The black box represents PP

Seas_Warming and 171.3 g/m·s for the Seas_Cooling. The moisture flux convergence differences over PP in MAM between the Seas_Warming and Seas_Cooling experiments were negative (-3.0×10^{-8} kg/(m^2·s), -6.0×10^{-8} kg/(m^2·s), -9.0×10^{-8} kg/(m^2·s)). The above results indicated that the positive sea–land thermal contrast increased the net water vapor fluxes across PP, moisture flux convergence over PP, and was conducive to the precipitation over PP.

Finally, the effect of sea–land thermal contrast along the Silk Road on spring precipitation over PP was investigated by calculating the simulated precipitation differences between CTL and Seas_Warming/Seas_Cooling (the latter minus the former). Figure 8a1, b1, c1 show that when SST over the five seas was warmed, the precipitation in MAM almost always increased over the entire study area, especially over the Mediterranean Sea, Black Sea, and Persian Gulf. Figure 8a2 shows that almost all the precipitation over PP was enhanced due to the increased sea–land thermal contrast. Figure 8b2 and c2 show that the precipitation over PP was also increased over most areas of PP in April and May, with a slight reduction over northern PP in April and over central PP in May due to the reduced moisture (Fig. 8b2). On the regional average over PP, the positive sea–land thermal contrast along the Silk Road increased the precipitation in MAM by 12.1 mm, 6.2 mm, and 26.0 mm, respectively. On the contrary, when the SST over the five seas was cooled, the precipitation over the study area were basically reduced, and the precipitation in MAM over PP decreased by 6.8 mm, 23.1 mm, and 12.5 mm, respectively. Therefore, the numerical simulation results also verified that the positive sea–land thermal contrast along the Silk Road increased the precipitation over PP due to the increased water vapor content and moisture fluxes across PP, and the negative sea–land thermal contrast reduced the precipitation over PP.

The differences between changing the land surface temperature and CTL were also analyzed. The differences of specific humidity (Fig. S15), water vapor flux (Table S1), water vapor budget (Fig. S16), and precipitation (Fig. S17) between Land_Warming and CTL were similar to those between Seas_Cooling and CTL, and the differences between Land_Cooling and CTL were similar to those between Seas_Warming and CTL, which indicated the consistent impacts of sea–land thermal contrast on the precipitation over Pamirs Plateau.

Based on above statistical analyses and the WRF model simulations, we proposed a conceptual model describing the impact of sea–land thermal contrast on the atmospheric circulations and moisture transport, which affected the precipitation over PP (Fig. 9). When the SST of the five seas were higher than the skin temperature of the Turan Plain, more water in the seas were heated, evaporated, and rose into the upper level. The evaporated water vapor was transported to PP by the westerlies, and finally more precipitation

was generated on the windward slope of the PP (Fig. 9a). When the SST of the five seas were lower than the skin temperature of the Turan Plain, limited soil moisture in the Turan Plain caused less water vapor evaporated. Although the water vapor was transported from the seas to the land at the low level, less water vapor reached PP, which resulted in less precipitation in PP (Fig. 9b).

4 Conclusions and discussion

This study analyzed the impact of sea–land thermal contrast along the Silk Road on the spring precipitation over PP. There were significant positive correlations between sea–land thermal contrast indices along the Silk Road and spring precipitation over PP from 1981 to 2018, indicating the positive effect of sea–land thermal contrast on spring precipitation over PP. Besides, the spatial distribution of correlations varied in March, April, and May. The areas with high correlation were in the central and southern PP in March, in the northwestern PP in April, and in the central and western PP in May.

A conceptual model describing the atmospheric circulations related to the sea–land thermal contrast along the Silk Road affecting the spring precipitation over PP was established. When the sea–land thermal contrast along the Silk Road was positive, more moisture evaporated from the seas to the upper level, and was transported to the PP along the westerlies, bringing abundant precipitation over PP. When the sea–land thermal contrast along the Silk Road was negative, the thermal circulation was beneficial to the transport of low–level water vapor from the seas to the land. However, part of moisture transported to the PP was lost due to the obstruction of the high terrain along the path, which eventually reduced precipitation over PP. The proposed framework was corroborated by the much lower pressure along the backward trajectories starting at PP in the years with positive sea–land thermal contrast and precipitation than in the years with negative sea–land thermal contrast and precipitation. Sensitivity experiments of WRF model results also indicated that the atmospheric circulations caused by the sea–land thermal contrast along the Silk Road led to evident spring precipitation enhancement over PP through changing the water vapor content along the moisture path arriving at PP and moisture fluxes across PP, which were consistent with the observations.

This study mainly discussed the influence of sea–land thermal contrast on precipitation at PP, and there are other factors affecting the sea–land thermal contrast by affecting the land thermal conditions. Zhou et al. (2021) showed that the declined soil moisture over drylands in the future changed the sea–land thermal contrast by regulating the evapotranspiration and atmospheric moisture transport. It is
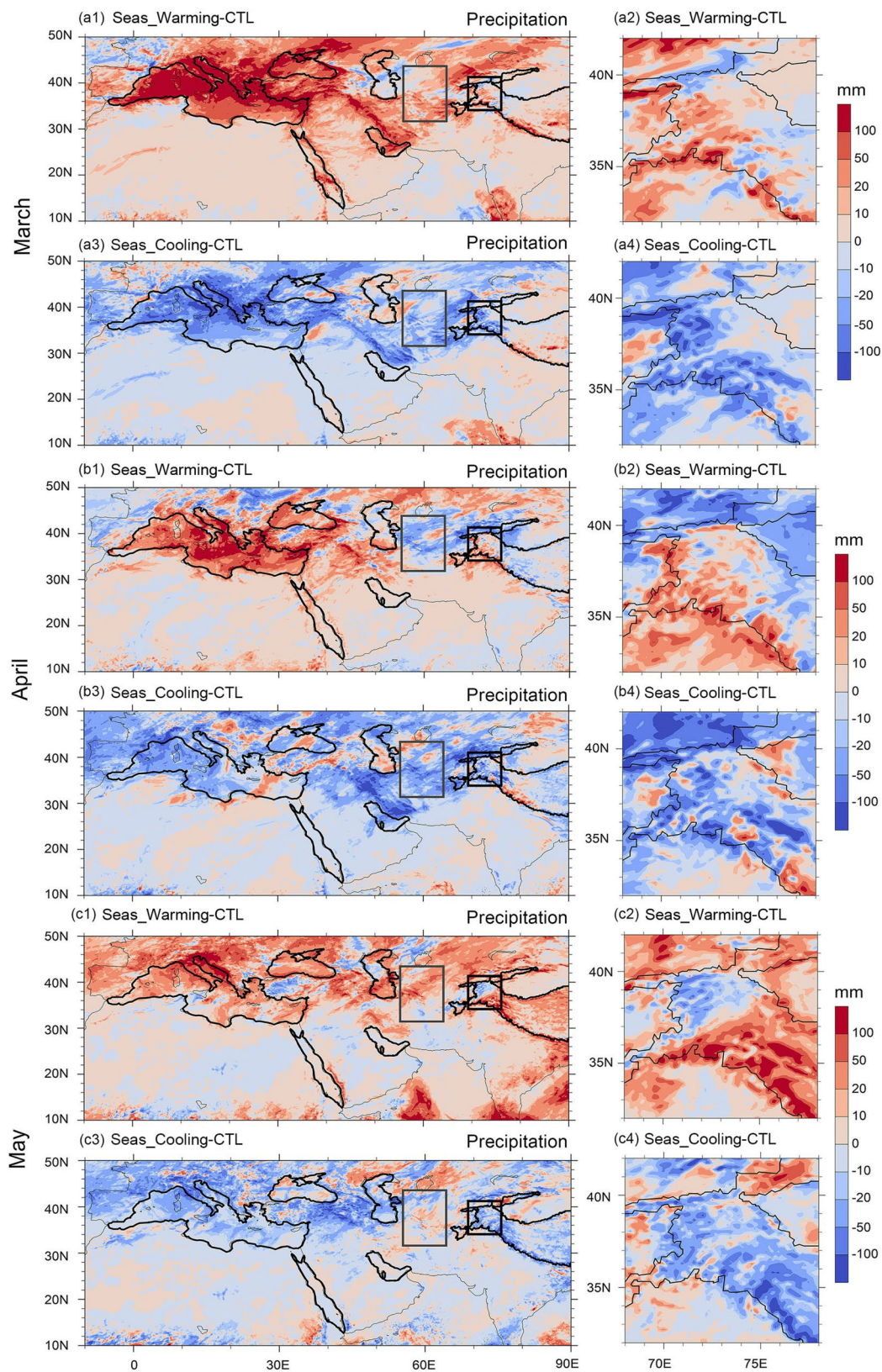
Fig. 8 Differences (SST sensitivity runs minus CTL run) in precipitation (mm) in MAM. The black lines represent the altitude contour line of 3000 m over TP and five seas. The gray box represents Turan Plain and the black box represents PP
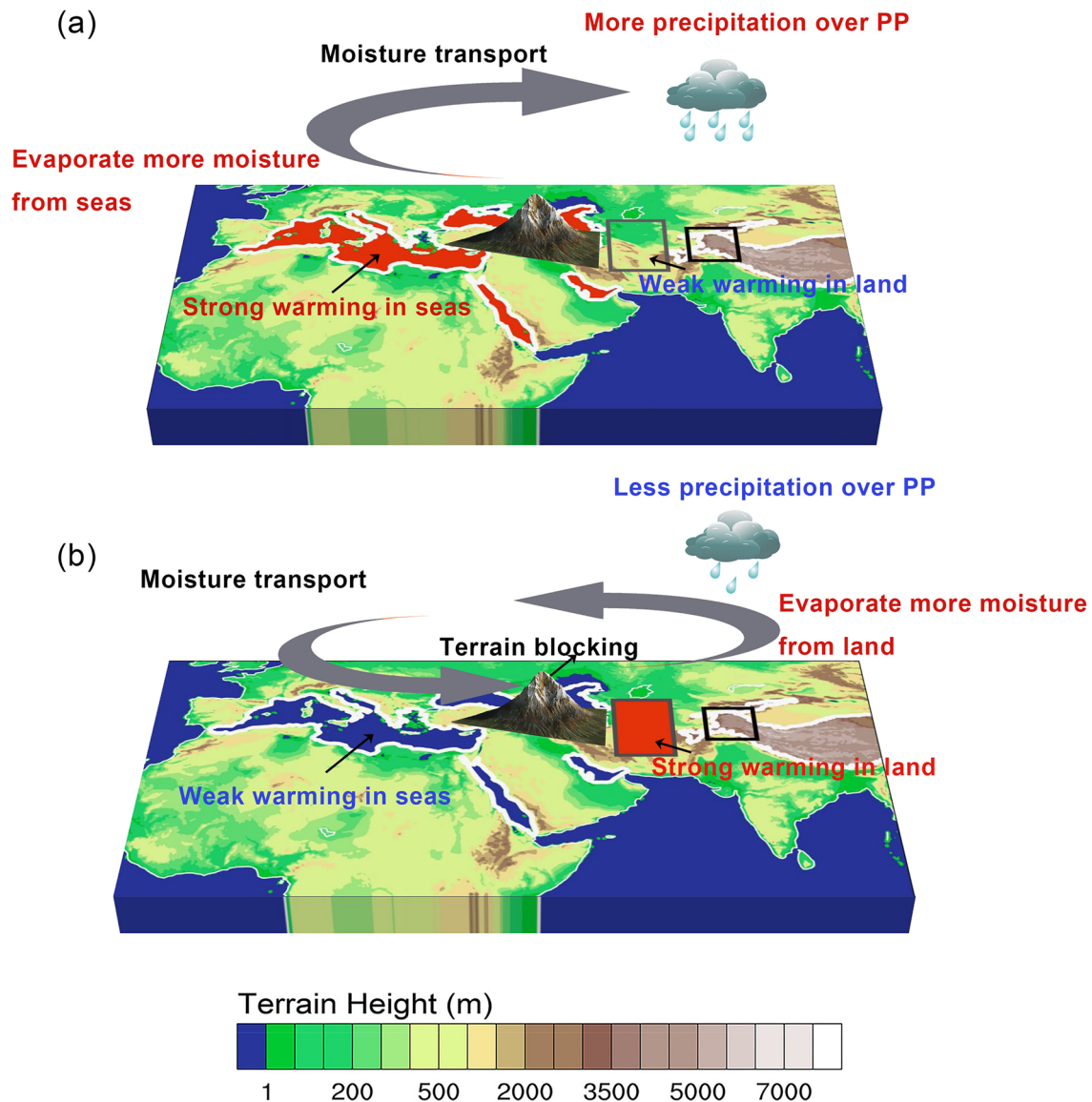
Fig. 9 A conceptual illustration of the atmospheric circulations when the sea–land thermal contrast along the Silk Road is **a** positive and **b** negative. Base map is the topography of the study area. The thick white lines represent the five seas and the altitude contour line of 3000 m over TP, and the gray box represents the Turan Plain

worth noting that soil moisture in Turan Plain is also closely related to precipitation over TP (He et al. 2022), while surface temperature and soil moisture interact with each other (Zhou et al. 2021, 2022). Table S2 shows that soil moisture and skin temperature in Turan Plain were significantly negatively correlated in March (− 0.54), April (− 0.72), and May (− 0.80). When the sea–land thermal contrast was positive, the increased soil moisture corresponded to the reduced skin temperature over Turan Plain, which enhanced the positive sea–land thermal contrast along the Silk Road, resulting in increased precipitation over PP. When the sea–land thermal contrast was negative, the increased soil moisture reduced the skin temperature over Turan Plain, which increased the

negative sea–land thermal contrast along the Silk Road, resulting in more precipitation over PP. The results indicate that soil moisture over Turan Plain positively affects precipitation over PP and the correlation coefficients between soil moisture in Turan Plain and precipitation over PP were 0.47–0.51 in MAM (Table S2). Moreover, the soil moisture could be affected by spring snow melt (Blankinship et al. 2014; Xu et al. 2020). We preliminarily analyzed the effect of spring snow melt on soil moisture over Turan Plain, and found that there was a significant positive correlation in March (0.58) and April (0.39) (Table S2). Therefore, the snow melt affects soil moisture and further changes skin temperature over Turan Plain, thus altering sea–land thermal

contrast along the Silk Road and ultimately affecting spring precipitation over PP.

This study used statistical analyses and numerical simulations to reveal the effect of sea–land thermal contrast along the Silk Road on spring precipitation over PP during 1981–2018. In the context of global warming, the sea–land thermal contrast along the Silk Road might change significantly due to the different warming rates of seas and land, and how the sea–land thermal contrast in the future affects the spring precipitation at PP needs further study.

Declarations

References

Aizen EM, Aizen VB, Melack JM et al (2001) Precipitation and atmospheric circulation patterns at mid-latitudes of Asia. Int J Climatol 21:535–556. https://doi.org/10.1002/joc.626

Bao J, Feng J, Wang Y (2015) Dynamical downscaling simulation and future projection of precipitation over China. J Geophys Res Atmos 120:8227–8243. https://doi.org/10.1002/2015JD023275

Becker A, Finger P, Meyer-Christoffer A et al (2013) A description of the global land-surface precipitation data products of the Global Precipitation Climatology Centre with sample applications including centennial (trend) analysis from 1901-present. Earth Syst Sci Data 5:71–99. https://doi.org/10.5194/essd-5-71-2013

Berg A, Lintner BR, Findell K et al (2015) Interannual coupling between summertime surface temperature and precipitation over land: processes and implications for climate change. J Clim 28:1308–1328. https://doi.org/10.1175/JCLI-D-14-00324.s1

Blankinship JC, Meadows MW, Lucas RG, Hart SC (2014) Snowmelt timing alters shallow but not deep soil moisture in the Sierra Nevada. Water Resour Res 50:1448–1456. https://doi.org/10.1002/2013WR014541

Boers N, Marwan N, Barbosa HMJ, Kurths J (2017) A deforestation-induced tipping point for the South American monsoon system. Sci Rep 7:41489. https://doi.org/10.1038/srep41489

Cai S, Huang A, Zhu K, Guo W, Wu Y, Gu C (2023) The forecast skill of the summer precipitation over Tibetan Plateau improved by the adoption of a 3D sub-grid terrain solar radiative effect scheme in a convection–permitting model. J Geophys Res Atmos 128:e2022JD038105. https://doi.org/10.1029/2022JD038105

Chen X, Wang S, Hu Z et al (2018) Spatiotemporal characteristics of seasonal precipitation and their relationships with ENSO in Central Asia during 1901–2013. J Geogr Sci 28:1341–1368. https://doi.org/10.1007/s11442-018-1529-2

Cheng H, Wu T, Dong W (2008) Thermal contrast between the middle-latitude Asian continent and adjacent ocean and its connection to the east Asian summer precipitation. J Clim 21:4992–5007. https://doi.org/10.1175/2008JCLI2047.1

Cohen JL, Furtado JC, Barlow M et al (2012) Asymmetric seasonal temperature trends. Geophys Res Lett 39:L04705. https://doi.org/10.1029/2011GL050582

Collins WD, Rasch PJ, Hack JJ et al (2004) Description of the NCAR Community Atmosphere Model (CAM3.0). Natl Cent for Atmos Res Ncar Koha Opencat. https://doi.org/10.5065/D63N21CH

Findell KL, Keys PW, Van Der Ent RJ et al (2019) Rising temperatures increase importance of oceanic evaporation as a source for continental precipitation. J Clim 32:7713–7726. https://doi.org/10.1175/JCLI-D-19

Gibson PB, Chapman WE, Altinok A et al (2021) Training machine learning models on climate model output yields skillful interpretable seasonal precipitation forecasts. Commun Earth Environ 2:159. https://doi.org/10.1038/s43247-021-00225-4

Hansen J, Ruedy R, Sato M, Lo K (2010) Global surface temperature change. Rev Geophys 48:RG4004. https://doi.org/10.1029/2010RG000345

He K, Liu G, Wu R et al (2022) Oceanic and land relay effects linking spring tropical Indian Ocean sea surface temperature and summer Tibetan Plateau precipitation. Atmos Res 266:105953. https://doi.org/10.1016/j.atmosres.2021.105953

Hong SY, Lim JOJ (2006) The WRF single–moment 6–class microphysics scheme (WSM6). Asia–Pac J Atmos Sci 42:129–151. https://api.semanticscholar.org/CorpusID:120362377

Hu P, Chen W, Chen SF, Liu YY, Wang L, Huang R (2021a) The leading mode and factors for coherent variations among the sub–systems of tropical Asian summer monsoon onset. J Clim 35:1597–1612. https://doi.org/10.1175/JCLI-D-21-0101.1

Hu S, Zhou TJ, Wu B (2021b) Impact of developing ENSO on Tibetan Plateau summer rainfall. J Clim 34:3385–3400. https://doi.org/10.1175/JCLI-D-20-0612.1

Huang W, Chen FH, Feng S, Chen JH (2013) Interannual precipitation variations in the mid–latitude Asia and their association with large–scale atmospheric circulation. Chinese Sci Bull 58:3962–3968. https://doi.org/10.1007/s11434-013-5970-4

Immerzeel WW, Lutz AF, Andrade M et al (2020) Importance and vulnerability of the world's water towers. Nature 577:364–369. https://doi.org/10.1038/s41586-019-1822-y

Janjic ZI (2001) Nonsingular implementation of the Mellor–Yamada level 2.5 scheme in the NCEP mesoscale model. National Centers for Environmental Prediction Office 437. https://repository.library.noaa.gov/view/noaa/11409

Jiang J, Zhou T (2023) Agricultural drought over water-scarce Central Asia aggravated by internal climate variability. Nat Geosci 16:154–161. https://doi.org/10.1038/s41561-022-01111-0

Jiang J, Zhou T, Chen X, Wu BO (1955) Central Asian precipitation shaped by the Tropical Pacific decadal variability and the Atlantic Multidecadal Variability. J Clim 34:7541–7553. https://doi.org/10.1175/JCLI-D-20

Juhlke TR, Meier C, van Geldern R et al (2019) Assessing moisture sources of precipitation in the Western Pamir Mountains (Tajikistan, Central Asia) using deuterium excess. Tellus B Chem Phys

Meteorol 71:1–16. https://doi.org/10.1080/16000889.2019.1601987

Mansfield LA, Nowack PJ, Kasoar M et al (2020) Predicting global patterns of long-term climate change from short-term simulations using machine learning. Npj Clim Atmos Sci 3:44. https://doi.org/10.1038/s41612-020-00148-5

Mao XL, Xing L, Shang W et al (2023) Moisture sources for precipitation over the Pamirs Plateau in winter and spring. Q J R Meteorol Soc. https://doi.org/10.1002/qj.4624

Mei Y, Maggioni V, Houser P et al (2020) A nonparametric statistical technique for spatial downscaling of precipitation over high mountain Asia. Water Resour Res 56:e2020WR027472. https://doi.org/10.1029/2020WR027472

Pohl E, Knoche M, Gloaguen R et al (2015) Sensitivity analysis and implications for surface processes from a hydrological modelling approach in the Gunt catchment, high Pamir Mountains. Earth Surf Dynam 3:333–362. https://doi.org/10.5194/esurf-3-333-2015

Rayner NA, Parker DE, Horton EB et al (2003) Global analyses of sea surface temperature, sea ice, and night marine air temperature since the late nineteenth century. J Geophys Res Atmos 108:4407. https://doi.org/10.1029/2002jd002670

Skamarock WC, Klemp JB, Dudjia J et al (2008) A description of the advanced research WRF version 3. NCAR Technical Note NCAR/TN–475+STR. Mesoscale and Microscale Meteorology Division. Natl Cent Atmos Res 475:1. https://doi.org/10.13140/RG.2.1.2310.6645

Stein AF, Draxler RR, Rolph GD et al (2015) Noaa's hysplit atmospheric transport and dispersion modeling system. B Am Meteorol Soc 96:2059–2077. https://doi.org/10.1175/BAMS-D-14-00110.1

Tian L, Jin J, Wu P et al (2020) High–resolution simulations of mean and extreme precipitation with WRF for the soil–erosive Loess Plateau. Clim Dyn 54:3489–3506. https://doi.org/10.1007/s00382-020-05178-6

Van Der Ent RJ, Savenije HHG, Schaefli B, Steele-Dunne SC (2010) Origin and fate of atmospheric moisture over continents. Water Resour Res 46:W09525. https://doi.org/10.1029/2010WR009127

Waheed U, Wang GJ, Gao ZQ et al (2021) Observed linkage between Tibetan Plateau soil moisture and South Asian summer precipitation and the possible mechanism. J Clim 34:361–377. https://doi.org/10.1175/JCLI-D-20-0347.1

Wang Z, Duan A, Yang S (2019) Potential regulation on the climatic effect of Tibetan Plateau heating by tropical air–sea coupling in regional models. Clim Dyn 52:1685–1694. https://doi.org/10.1007/s00382-018-4218-z

Wang X, Chen Y, Fang G et al (2022) The growing water crisis in Central Asia and the driving forces behind it. J Clean Prod 378:134574. https://doi.org/10.1016/j.jclepro.2022.134574

Wu R, Liu G, Ping Z (2014) Contrasting Eurasian spring and summer climate anomalies associated with western and eastern Eurasian spring snow cover changes. J Geophys Res 119:7410–7424. https://doi.org/10.1002/2014JD021764

Xu B, Chen H, Gao C et al (2020) Abnormal change in spring snowmelt over Eurasia and its linkage to the East Asian Summer Monsoon: the hydrological effect of snow cover. Front Earth Sci 8:594656. https://doi.org/10.3389/feart.2020.594656

Xue Y, De Sales F, Lau WK-M et al (2016) West African monsoon decadal variability and drought and surface-related forcings: Second West African Monsoon Modeling and Evaluation Project Experiment (WAMME II). Clim Dyn 47:3517–3545. https://doi.org/10.1007/s00382-016-3224-2

Xue Y, Diallo I, Li W et al (2018) Spring land surface and subsurface temperature anomalies and subsequent downstream late spring-summer droughts/floods in North America and East Asia. J Geophys Res Atmos 123:5001–5019. https://doi.org/10.1029/2017JD028246

Yana LI, Yang S, Deng Y, Zheng B (2020) Signals of spring thermal contrast related to the interannual variations in the onset of the South China sea summer monsoon. J Clim 33:27–38. https://doi.org/10.1175/JCLI-D-19-0174.1

Yang J, Chen H (2022) Influences of spring land surface thermal anomalies over West Asia on Indian Early Summer Monsoon activity and its pathway. J Clim 35:6051–6074. https://doi.org/10.1175/JCLI-D-21-0916.1

Yang J, Chen H, Song Y et al (2021) Atmospheric circumglobal teleconnection triggered by spring land thermal anomalies over West Asia and its possible impacts on early summer climate over Northern China. J Clim 34:5999–6021. https://doi.org/10.1175/JCLI-D-20

Yao YL, Zou XQ, Zhao YF, Wang T (2019) Rapid changes in land-sea thermal contrast across China's coastal zone in a warming climate. J Geophys Res Atmos 124:2049–2067. https://doi.org/10.1029/2018JD029347

Yu W, Liu Y, Yang XQ et al (2021) Impact of North Atlantic SST and Tibetan Plateau forcing on seasonal transition of springtime South Asian monsoon circulation. Clim Dyn 56:559–579. https://doi.org/10.1007/s00382-020-05491-0

Zaitchik BF, Evans JP, Smith RB (2007) Regional impact of an elevated heat source: the Zagros Plateau of Iran. J Clim 20:4133–4146. https://doi.org/10.1175/JCLI4248.1

Zhang P, Duan A (2021) Dipole mode of the precipitation anomaly over the Tibetan Plateau in Mid-Autumn associated with Tropical Pacific-Indian Ocean Sea surface temperature anomaly: role of convection over the Northern Maritime Continent. J Geophys Res Atmos 126:e2021JD034675. https://doi.org/10.1029/2021JD034675

Zhang J, Wang WC, Leung LR (2008) Contribution of land-atmosphere coupling to summer climate variability over the contiguous United States. J Geophys Res Atmos 113:D22109. https://doi.org/10.1029/2008JD010136

Zhao Y, Zhang H (2016) Impacts of SST Warming in tropical Indian Ocean on CMIP5 model-projected summer rainfall changes over Central Asia. Clim Dyn 46:3223–3238. https://doi.org/10.1007/s00382-015-2765-0

Zhao P, Jiang PP, Zhou XJ, Zhu CW (2009) Modeling impacts of East Asian ocean-land thermal contrast on spring southwesterly winds and rainfall in eastern China. Chin Sci Bull 54:4733–4741. https://doi.org/10.1007/s11434-009-0229-9

Zhou S, Williams AP, Lintner BR et al (2021) Soil moisture–atmosphere feedbacks mitigate declining water availability in drylands. Nat Clim Chang 11:38–44. https://doi.org/10.1038/s41558-020-00945-z

Zhou S, Williams AP, Lintner BR et al (2022) Diminishing seasonality of subtropical water availability in a warmer world dominated by soil moisture–atmosphere feedbacks. Nat Commun 13:5756. https://doi.org/10.1038/s41467-022-33473-9

Zhou P, Shao M, Ma M et al (2023) WRF gray–zone dynamical downscaling over the Tibetan Plateau during 1999–2019: model performance and added value. Clim Dyn 61:1371–1390. https://doi.org/10.1007/s00382-022-06631-4